Front. Energy
https://doi.org/10.1007/s11708-020-0667-2

RESEARCH ARTICLE

Xiashuang LUO, Yangge GUO, Hongru ZHOU, Huan REN, Shuiyun SHEN, Guanghua WEI, Junliang ZHANG

Thermal annealing synthesis of double-shell truncated octahedral Pt-Ni alloys for oxygen reduction reaction of polymer electrolyte membrane fuel cells

Abstract Shape-controlled Pt-Ni alloys usually offer an exceptional electrocatalytic activity toward the oxygen reduction reaction (ORR) of polymer electrolyte membrane fuel cells (PEMFCs), whose tricks lie in well-designed structures and surface morphologies. In this paper, a novel synthesis of truncated octahedral $PtNi_{3.5}$ alloy catalysts that consist of homogeneous Pt-Ni alloy cores enclosed by NiO-Pt double shells through thermally annealing defective heterogeneous $PtNi_{3.5}$ alloys is reported. By tracking the evolution of both compositions and morphologies, the outward segregation of both PtO_x and NiO are first observed in Pt-Ni alloys. It is speculated that the diffusion of low-coordination atoms results in the formation of an energetically favorable truncated octahedron while the outward segregation of oxides leads to the formation of NiO-Pt double shells. It is very attractive that after gently removing the NiO outer shell, the dealloyed truncated octahedral core-shell structure demonstrates a greatly enhanced ORR activity. The as-obtained truncated octahedral $Pt_{2.1}Ni$ core-shell alloy presents a 3.4-folds mass-specific activity of that for unannealed sample, and its activity preserves 45.4% after 30000 potential cycles of accelerated degradation test (ADT). The peak power density of the dealloyed truncated octahedral $Pt_{2.1}Ni$ core-shell alloy catalyst based membrane electrolyte assembly (MEA) reaches 679.8 mW/cm^2, increased by 138.4 mW/cm^2 relative to that based on commercial Pt/C.

Keywords dealloyed Pt-Ni alloys, truncated octahedron, double-shell, thermal annealing, oxygen reduction reaction (ORR)

Received Nov. 20, 2019; accepted Feb. 5, 2020; online Jul. 10, 2020

Xiashuang LUO, Yangge GUO, Shuiyun SHEN
Institute of Fuel Cells, School of Mechanical Engineering, Shanghai Jiao Tong University, Shanghai 200240, China

Hongru ZHOU, Huan REN
Shanghai Hydrogen Propulsion Technology Co., Ltd, Shanghai 201804, China

Guanghua WEI
SJTU-Paris Tech Elite Institute of Technology, Shanghai Jiao Tong University, Shanghai 200240, China

Junliang ZHANG (✉)
Institute of Fuel Cells, School of Mechanical Engineering, MOE Key Laboratory for Power Machinery and Engineering, Shanghai Jiao Tong University, Shanghai 200240, China
E-mail: junliang.zhang@sjtu.edu.cn

1 Introduction

The kinetically sluggish oxygen reduction reaction (ORR) rate in the cathode of low-temperature polymer electrolyte membrane fuel cells (PEMFCs) leads to a huge voltage loss during operation and requires a high Pt loading, which is scarce and expensive, thus greatly increasing fuel cell cost and impeding the large-scale application of fuel cell vehicles [1]. According to the latest analysis from Annual Merit Review and Peer Evaluation Meeting, the catalyst cost is projected to be the largest part (approximately 41%) in a PEMFC stack [2]. Therefore, various effective strategies on developing more active Pt-based catalysts should be explored to reduce the amount of Pt for the cathodic ORR without compromising fuel cell performance. So far, most researches focus on designing advanced Pt-M (M = Fe, Co, Ni, Cu, Zr, Y, etc.) alloys as well as core-shell Pt monolayer catalysts, which are anticipated to ideally maximize the Pt utilization. The alloy of Pt with 3d-transition metals M (M = Fe, Co, Ni, Cu, etc.) will significantly improve the ORR activity via the ensemble effect, the electronic and/or the strain effect [3,4]. Thereinto, the Pt-Ni bimetallic alloy catalysts are regarded as excellent electrocatalysts toward the ORR of PEMFCs. Indeed, the ORR activity of the series of Pt-M alloy catalysts depends on surface composition and morphology [5]. More attractively, there is no doubted

that crystalline orientations have played an extraordinary role in increasing the ORR activity [6–10]. Very recently, more and more efforts have been dedicated to synthesizing shape-controlled Pt-M alloy nanocrystals with special facets exposed, especially the types of Pt-Ni alloys with {111} facets [11–20].

Cui et al. [13] reported the synthesis of octahedral PtNi nanoparticles (NPs) using a self-surfactant method, in which the precursor ligands of acetyl acetonate determined the formation of octahedral shape rather than the interaction of the solvent N, N-Dimethylformamide (DMF) with {111} facets. The as-obtained PtNi octahedral with a size of 9.5 nm demonstrated a mass activity of 1.45 A/mg_{Pt}. Wu et al. [20] generated Pt-based icosahedral nanocrystals with surfaces enclosed by {111} facets through a gas reducing agent in liquid solution (GRAILS) method which used both CO gas and capping agents for shape controlling. Among the as-obtained Pt-M (M = Au, Ni, Pd) alloys, Pt_3Ni icosahedral nanocrystals present an impressive mass-specific activity of 0.62 A/mg_{Pt}. Zhang et al. [18] *in situ* produced carbon supported octahedral Pt-Ni alloys with an improved mass activity of 1.96 A/mg_{Pt} by reducing metal acetylacetonates impregnated on carbon support in both CO and H_2 gases.

In addition to directly generating shape-controlled Pt-M alloy NPs, the surface composition and morphology of Pt-M alloys can also be accurately controlled by adjusting the degree of surface segregation of transition metals in after-treatment, especially thermal annealing. Beermann et al. [21] investigated the impact of annealing temperature on the composition and shape of Pt-Ni based NPs through annealing Pt-Ni based NPs with Ni-rich {111} facets under 4% hydrogen at 300°C. It was observed that the NPs obtained with Ni located more on the inside present both an enhanced reactivity (2.7 A/mg_{Pt}) and durability. Chen et al. [22] synthesized hollow Pt_3Ni frames consisting of 24 edges of parent rhombic dodecahedron and found that the formation of Pt-skin-terminated {111}-like surface structure led to an extraordinary high mass activity of 5.7 A/mg_{Pt}. They obtained Pt_3Ni nanoframes via eroding segregated NiO in $PtNi_3$ polyhedrons in nonpolar solvents, and employed oxygen in this method for the oxidation and segregation of Ni from $PtNi_3$ polyhedrons. Wang et al. [23] reported the achievement of ordered Pt_3Co NPs with 2–3 atomic-layer-thick Pt shells through transferring disordered Pt-Co alloy under H_2/N_2 mixed gas atmosphere at 700°C which presented a 2-folds mass-specific activity compared with disordered Pt_3Co alloys as well as commercial Pt/C. They also observed surface segregated Co/Co oxides during the preparation. Moreover, it was also pointed out that the Pt surface diffusion during thermal annealing could tailor the surface composition, thus forming Pt-rich shells [24,25]. It is thus believed that thermal annealing is an effective after-treatment strategy for achieving ideal surface elemental distribution and morphology in Pt-M alloys.

In this regard, herein, heterogeneous quasi-octahedral Ni-rich Pt-based alloys were first synthesized using a one-step method. Then, the alloys were annealed in H_2 atmosphere to form a core-double-shells structure without changing their octahedral morphology. It was proved that the as-obtained truncated octahedral $PtNi_{3.5}$ alloys were well-shaped and consisted of homogeneous Pt-Ni alloy cores enclosed by NiO-Pt double shells. The removal of NiO outer-shell could be considered as a novel dealloying method without morphological changes in Ni-rich Pt-based alloys. After being dealloyed, the ORR activity of the annealed truncated octahedral $Pt_{2.1}Ni$ electrocatalyst was 2.91 mA/cm^2 and 1.24 A/mg_{Pt} in area- and mass-specific activity, which were 4.2 and 3.4 times that of unannealed defective quasi-octahedral Pt_3Ni. When being applied in a membrane electrolyte assembly (MEA) with 0.1 mg/cm^2 Pt loading employed, the current density at 0.6 V and the maximum power density of annealed truncated octahedral $Pt_{2.1}Ni$ were increased by 498 mA/cm^2 and 138.4 mW/cm^2 compared with that of commercial Pt/C.

2 Experiment

2.1 Synthesis of NPs

To prepare the as-prepared $PtNi_{3.5}/C$, a certain molar ratio of $Pt(acac)_2$ (Sigma-Aldrich, 97%) and $Ni(acac)_2$ (Sigma-Aldrich, 95%) powders were mixed with Vulcan XC72R carbon black, and then dispersed in DMF (Alfa-Aesar, 99.8%) by sonication. The mixture was sealed in a reactor and heated to 120°C for 40 h. When the suspension was cooled to room temperature, the solids were separated by centrifugation, and the waste liquid was removed. An equal volume ratio of alcohol and chloroform was mixed as the cleaning agent, in which the solids were dispersed by centrifugation and separated for three times. After that, the sediments were further dispersed in alcohol and washed for five times, followed by desiccation in the vacuum oven. Part of the obtained carbon-supported catalysts were first treated with the volume fraction of 20% acetic acid under 80°C for 1 h, washed by ultrapure water for three times and stoved in the vacuum oven. Others were first annealed at 300°C with a heating rate of 10°C/min in H_2 (5 vol% in Ar) or pure Ar for 90 min. Then the catalysts annealed under H_2 (5 vol% in Ar) were applied a similar acid pickling with the unannealed sample. The synthetic methods for different Pt-Ni catalysts mentioned in Section 3 were summarized in Table 1.

2.2 Electrochemical measurements

The electrochemical measurements were performed in a three electrodes system at room temperature, employing a glassy carbon rotating electrode (area: 0.196 cm^2) with a thin film of the catalysts as the working electrode. A

Table 1 Synthetic methods for different Pt-Ni catalysts

Sample	Synthetic method
As-prepared $PtNi_{3.5}$/C	The $PtNi_{3.5}$ NPs were *in situ* deposited on carbon powders through solvothermal synthesis
Acid-treated Pt_3Ni/C	An acid pickling was applied to as-prepared $PtNi_{3.5}$/C
Annealed$_{5\%\ H_2}$ $PtNi_{3.5}$/C	Thermally annealed as-prepared $PtNi_{3.5}$/C under H_2 (5 vol% in Ar)
Acid-treated annealed$_{5\%\ H_2}$ $Pt_{2.1}Ni$/C	An acid pickling was applied to annealed$_{5\%\ H_2}$ $PtNi_{3.5}$/C
Annealed$_{5\%\ H_2}$ acid-treated Pt_3Ni/C	Thermally annealed the acid-treated Pt_3Ni/C under H_2 (5 vol % in Ar)
Annealed$_{Ar}$ $PtNi_{3.5}$/C	Thermally annealed as-prepared $PtNi_{3.5}$/C under pure Ar

calomel electrode and Pt plate were used as a reference and counter electrode. The reference electrode was calibrated and converted to reversible hydrogen electrode (RHE). To prepare the thin film, 4 μL catalyst ink of isopropanol comprising 0.3 mg Pt contents per milliliter was applied to the glassy carbon rotating electrode. The working electrode was dried in the open air and then 4 μL nafion solution diluted by 2 μL of 20 wt% nafion solution (DuPont) per milliliter was loaded on the thin film of the catalysts before electrochemical measurements. Electrochemical experiments were conducted on a CHI-660 potentiostat with a rotating disk electrode (RDE) system (Pine Research Instruments) at room temperature. 0.1 mol/L $HClO_4$ (Sigma-Aldrich, 70%) solution prepared with ultrapure water was used as electrolyte in the electrolytic cell.

The film of the catalysts were activated by applying potential cycling between 0.1 and 1.1 V (versus RHE) at 0.5 V/s for 200 cycles to obtain a stable current-voltage curve in the N_2-saturated $HClO_4$ solution, and the cyclic voltammetry (CV) curves were recorded by scanning the potential in the same voltage range at 20 mV/s for 10 cycles. The electrochemical surface area (ECSA) was evaluated by integrating the area for the adsorption/desorption of hydrogenated species in the CV curve, and using a conversion factor of 210 μC/cm^2. Then, at a speed of 1600 r/min, the ORR polarization curves were recorded by scanning the potential from 0.2 V to 1.1 V (vs RHE) at 10 mV/s in the saturated $HClO_4$ solution of O_2. The kinetic current can be calculated using the *Koutecky-Levich equation* with the measured current (at 0.9 V versus RHE) and the diffusion limited current obtained from the linear sweep voltammetry (LSV) curves. The accelerated degradation tests (ADT) were taken in the N_2-saturated $HClO_4$ solution by scanning the potential between 0.6 and 1.0 V (versus RHE) at 0.1 V/s. The ORR curves were recorded after 5000 cycles for the acid-treated Pt_3Ni/C and after 3000, 5000, 12000, 20000, and 30000 cycles for the acid-treated annealed$_{5\%\ H_2}$ $Pt_{2.1}Ni$/C.

2.3 Single-cell tests

The acid-treated Pt_3Ni/C, the acid-treated annealed$_{5\%\ H_2}$ $Pt_{2.1}Ni$/C, and commercial Pt/C (TKK, 46.7%) were employed as the cathodic catalysts while commercial Pt/C applied as anidic catalyst with 0.1 mg/cm^2 Pt loading in both sides of a Nafion 211 membrane (DuPont). Catalyst inks were applied to the membrane through electrostatic spray to form a thin film of the catalysts with active areas measuring 4 cm^2. Single cell tests were then conducted using a fuel cell test station (Fuelcon test station, Evaluator-C). The single cells were maintained at 80°C throughout the experiment and the relative humidity (RH) was fixed at 100%. To activate the MEAs, voltage loads were applied while supplying hydrogen to the anode (300 sccm) and oxygen (600 sccm) to the cathode. The voltage was maintained for 5, 10, and 10 min at 0.8, 0.6, and 0.4 V. This process was repeated several times until the voltage and current remained constant. The cathodic gas was then changed from O_2 to air (600 sccm) and the initial performances of the MEAs bearing different cathodic catalysts were evaluated at 0.5 bar back-pressure.

2.4 Characterization

An iCAP6300 inductively coupled plasma (ICP) Optical was chosen for ICP elemental analyses. Transmission electron microscope (TEM) and high resolution-transmission electron microscope (HR-TEM) images were collected on a JEOL 2100F field emission microscope. High angle annular dark field-scanning transmission electron microscopy (HAADF-STEM) images and energy dispersive X-ray spectroscopy (EDX)-mapping results were acquired on a JEOL JEM-ARM 200F spherical aberration correction TEM equipped with EDX functionality. X-ray diffraction (XRD) patterns were recorded on a D8 ADVANCE Da Vinci (3 kW). X-ray photoelectron spectroscopy (XPS) spectrums were obtained on an AXIS UltraDLD.

3 Results and discussion

The $PtNi_{3.5}$ NPs were *in situ* deposited on carbon powders in DMF and the product is labeled "as-prepared $PtNi_{3.5}$/C" (Section 2, Table 1). Figures 1(a-1) and 1(a-2) show both TEM and HR-TEM images of the as-prepared $PtNi_{3.5}$/C. It is observed that most as-prepared $PtNi_{3.5}$ NPs are composed of defective quasi-octahedrons with an average edge length of 10.28 nm. The defective structure including evident curving edges and surface depressions could lead to the exposure of many low-coordination sites. To gain an

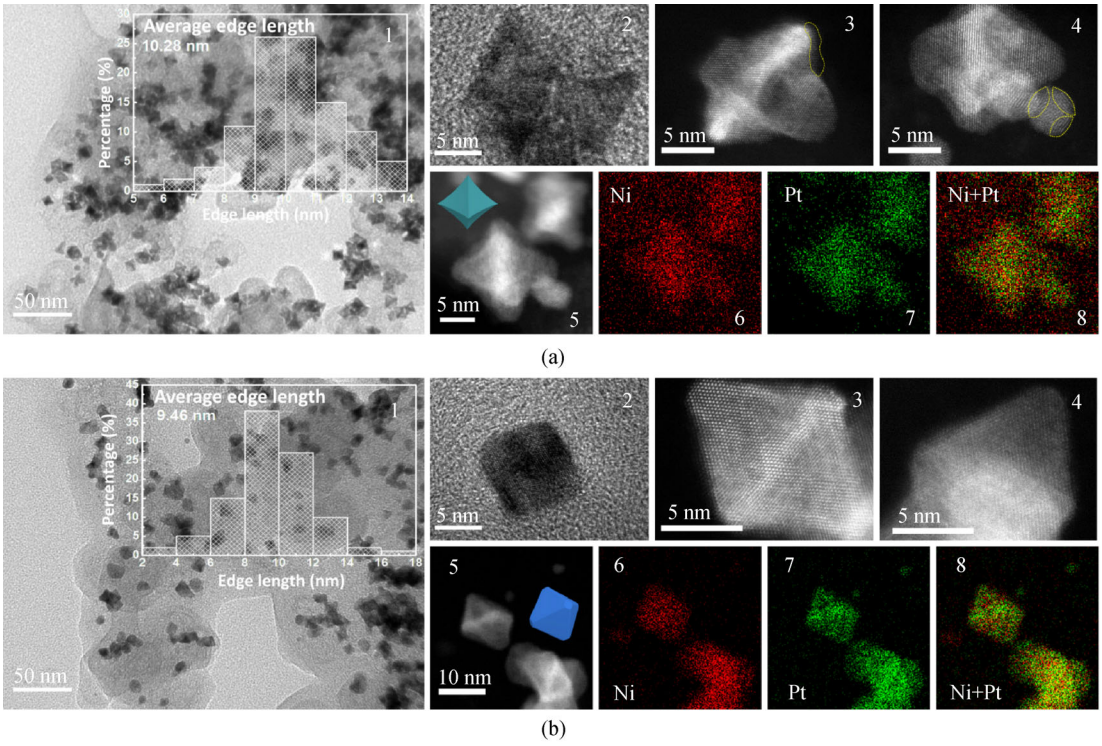

1—TEM images; 2—HR-TEM images; 3, 4—atomic-resolution HAADF-STEM images viewed along [110] zone axis; 5—HAADF-STEM images; 6—STEM EDX-mappings of Ni; 7—STEM EDX-mappings of Pt; 8—STEM EDX-mappings of the composite Ni versus Pt

Fig. 1 Morphology and elemental distribution analysis. (a) As-prepared $PtNi_{3.5}$/C; (b) annealed$_{5\%\ H_2}$ $PtNi_{3.5}$/C.

insight into delicate composition profiles, HAADF-STEM was also employed to characterize the as-prepared $PtNi_{3.5}$ NPs. Figure 1(a-5) depicts the HAADF-STEM image, whose corresponding elemental mappings are presented in Figs. 1(a-6) to (a-8). The two-dimensional mappings of Pt and Ni elements in representative as-prepared $PtNi_{3.5}$ NPs are characterized with identical variations, demonstrating a simultaneous distribution of Pt and Ni in the NPs.

Figure 1(b-1) presents the morphology of the sample resulting from thermally annealing the as-prepared $PtNi_{3.5}$/C under H_2 (5 vol% in Ar) at 300°C for 90 min. A pure Ar atmosphere was also employed to treat the as-prepared $PtNi_{3.5}$/C for comparison. The morphology and the elemental distribution for the as-obtained samples are collected in Fig. S1 (Electronic supplementary material (ESM)). The above-annealed electrocatalysts are labeled as "annealed$_{gas}$ $PtNi_{3.5}$" with "gas" corresponding to the annealing atmosphere. Based on Fig. 1(b-1) and Fig. S1(a), it is observed that although the alloy NPs both exhibit distinct structure changes after being annealed under either 5 vol% H_2 in Ar or pure Ar, most annealed NPs with a size of 4 nm or larger in edge length remain enclosed with eight {111} facets. The average edge length is 9.46 nm for the annealed$_{5\%\ H_2}$ $PtNi_{3.5}$ but 8.95 nm for the annealed$_{Ar}$ $PtNi_{3.5}$. To figure out the changes of surface structure, both the annealed$_{5\%\ H_2}$ and the annealed$_{Ar}$ $PtNi_{3.5}$ NPs were further analyzed under HR-TEM. As shown in Fig. 1(b-2) and Figs. S1(b) and S1(c), the structure defects disappear after thermal anneal, and flat {100} and {111} facets are formed instead. A thermodynamically driven effect for the morphological restructure is confirmed as identical structure formed after thermal anneal regardless of annealing gaseous atmosphere. It is believed that the unsteady low-coordination edge atoms have a priority to transform in order to lower the surface energy, and the edge atoms diffusing toward {111} facets could fill the depression on surfaces, thus resulting in more focused bulks and smooth {111} facets. The structure described as truncated octahedron is energetically favorable with the formation of {100} facets, as predicted by Wang et al. [26]. The element distribution of Pt and Ni inside the annealed$_{5\%\ H_2}$ $PtNi_{3.5}$ NPs were determined by STEM-EDX elemental face-scanning. The elemental maps of projected Pt and Ni are recorded in Figs. 1(b-5) to (b-8), which implies the formation of Pt segregation as well as a uniform distribution of Ni in the annealed$_{5\%\ H_2}$ $PtNi_{3.5}$ NPs. On the contrary, no segregation of Pt or Ni is observed in the annealed$_{Ar}$ $PtNi_{3.5}$ NPs (Figs. S1(d)–S1(g) in ESM). It is

therefore concluded that the elemental distribution change is driven by a gaseous atmosphere effect. Apart from the well-shaped truncated octahedrons, some small particles are also visible in Fig. 1(b-5). After being annealed under the H_2 environment, they remain spheroid in morphology and monodisperse while enclosed with Ni-rich shells.

The delicate chemical composition at the atomic scale was further observed under STEM. Figures 1(a-3) and 1(a-4), 1(b-3) and 1(b-4) show the atomic-resolution HAADF-STEM images viewed along [110] zone axis of individual as-prepared and annealed$_{5\%\ H_2}$ $PtNi_{3.5}$ NPs. The structure defects can be further confirmed in the as-prepared $PtNi_{3.5}$ NPs with rounded vertices and loss of {111} facets (Figs. 1 (a-3) and 1(a-4)). Usually, those concave-like surface defects could act as catalytic sites with unique activities due to their unique local structural environments [27]. However, it is also noted that the as-prepared $PtNi_{3.5}$ crystals can be either homogeneous or heterogeneous as the presence of anisotropic crystal orientations (region inside the yellow line). Compared with homogeneous crystals, those heterogeneous crystals are thermodynamically unstable because of the presence of defects on grain surfaces and boundaries which will increase the internal energy, thus leading to the fact that the anisotropic quasi-octahedrons are easily to be destroyed under the cathode operating condition. From Figs. 1(b-3) and 1(b-4), the morphological restructure under H_2 (5 vol% in Ar) atmosphere results in the formation of atomically flat {111} and {100} facets. It is noted that the HAADF-STEM technique has a high compositional sensitivity when there are equal thickness effects, therefore, the segregation of Pt or Ni could be distinguished through *Z*-contrast [28]. The uniform contrast in the center of atomic-resolution images confirms a relative high alloy degree inside the annealed$_{5\%\ H_2}$ $PtNi_{3.5}$ truncated octahedrons. It is also observed that the bimetallic cores are enclosed with double shells, evidenced by the outer two layers with a weaker *Z*-contrast enriched by Ni and the following four layers with stronger *Z*-contrast enriched by Pt. It is thus believed that the annealed$_{5\%\ H_2}$ $PtNi_{3.5}$ truncated octahedron possess a homogeneous Pt-Ni alloy core surrounded by two shells, one being Ni-segregated outer shell, and the other, Pt-segregated inner shell.

It is noted that the transition metal Ni-segregated outer shells of the annealed$_{5\%\ H_2}$ $PtNi_{3.5}$ truncated octahedrons are unstable and will dissolve during electrochemical measurements or single-cell tests. Then, the as-dissolved Ni ions can block the gas diffusion layer pores as well as change the conductivity of membrane [29]. Therefore, an acid pickling was applied to the annealed$_{5\%\ H_2}$ $PtNi_{3.5}$/C before electrochemical measurements. The same acid treatment was also conducted on the as-prepared $PtNi_{3.5}$/C for comparison. After removing the surface oxides and unstable heterogeneous structures, the ICP results point out that the acid treatment for the as-prepared $PtNi_{3.5}$/C and annealed$_{5\%\ H_2}$ $PtNi_{3.5}$/C leads to the formation of Pt_3Ni/C (labeled "acid-treated Pt_3Ni/C") and $Pt_{2.1}Ni$/C (labeled "acid-treated annealed$_{5\%\ H_2}$ $Pt_{2.1}Ni$/C"). Since the annealed$_{5\%\ H_2}$ $PtNi_{3.5}$/C truncated octahedrons have Pt-segregated inner shells, it is more difficult for the Ni elements in the bimetallic core to dissolve.

The elemental analyses based on XPS were performed to determine the valence state of near-surface atoms. As shown in Figs. 2(a)–2(d), XPS spectra from the Ni 2p core level regions of the as-prepared $PtNi_{3.5}$, the acid-treated Pt_3Ni, the annealed$_{5\%\ H_2}$ $PtNi_{3.5}$, and the acid-treated annealed$_{5\%\ H_2}$ $Pt_{2.1}Ni$ were fitted with four doublets corresponding to Ni^0, Ni^{2+} and their satellite peaks. It is seen that the Ni element on the surfaces of the as-prepared $PtNi_{3.5}$ is mainly in the form of Ni^{2+} , which is twice the amount of Ni^0 (Table S1, in ESM). Combining with the O 1s spectra, it can be confirmed that a large amount of NiO was formed in the as-prepared $PtNi_{3.5}$ NPs during the hydrothermal process. From Table S1, it is also observed that after H_2 annealing, the proportion of NiO slightly decreases, which implies that NiO has been marginally reduced during the H_2 annealing process. Undoubtedly, after the acid treatment, the majority of NiO has been removed in the acid-treated annealed$_{5\%\ H_2}$ $Pt_{2.1}Ni$/C near-surface regions while there exists only a slight decrease in NiO/Ni ratio in the acid-treated Pt_3Ni/C. It can thus be certain that a segregation of NiO toward surfaces and the formed Ni rich outer shells of the annealed$_{5\%\ H_2}$ $PtNi_{3.5}$ NPs are mainly composed of NiO. It is also important to mention that the migration and agglomeration of Pt-Ni alloy NPs on carbon powders is simultaneously accompanied with internal structural deformation, which will

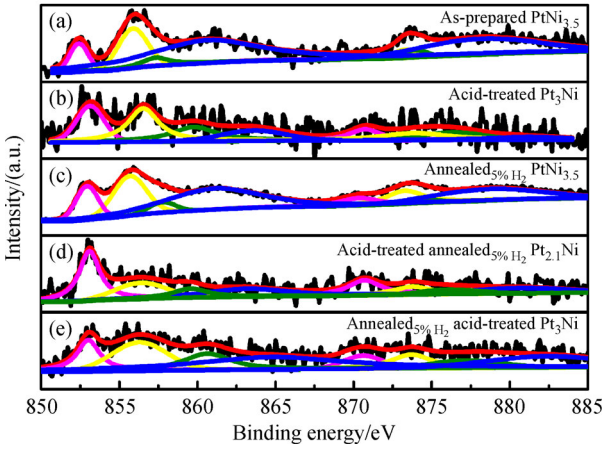

Fig. 2 Ni 2p XPS spectra (black), the doublets corresponding to Ni^0 (pink), Ni^{2+} (yellow) and their satellite peaks (green and blue, respectively) as well as the fitting results (red).
(a) As-prepared $PtNi_{3.5}$; (b) acid-treated Pt_3Ni; (c) annealed$_{5\%\ H_2}$ $PtNi_{3.5}$; (d) acid-treated annealed$_{5\%\ H_2}$ $Pt_{2.1}Ni$; (e) annealed$_{5\%\ H_2}$ acid-treated Pt_3Ni.

therefore result in the loss of ECSA for ORR [30]. It has been well acknowledged that the formation of oxide shells such as iron oxides [31], MgO [32], and NiO [33] can successfully prevent the sintering of NPs. It is thus believed that the NiO-segregated outer shells on the annealed$_{5\%\ H_2}$ $PtNi_{3.5}$/C play an important role in mitigating conglobation during internal structural deformation.

To further identify the formation and effect of formed NiO-segregated outer shells during the H_2 anneal process, the acid-treated Pt_3Ni/C was annealed under the same conditions with that for the as-prepared $PtNi_{3.5}$/C (labeled "annealed$_{5\%\ H_2}$ acid-treated Pt_3Ni/C"). The Ni 2p XPS spectra of the annealed$_{5\%\ H_2}$ acid-treated Pt_3Ni/C was collected in Fig. 2(e). Compared with Fig. 2(b), the Ni 2p XPS spectra of the annealed$_{5\%\ H_2}$ acid-treated Pt_3Ni confirms a promotion in the ratio of NiO under a reducing environment, which indicates a common phenomenon of NiO segregation for the thermal anneal under a H_2 gaseous environment, irrespective to the proportion of Pt and Ni in the NPs. The TEM images of the acid-treated Pt_3Ni/C, the acid-treated annealed$_{5\%\ H_2}$ $Pt_{2.1}Ni$/C, and the annealed$_{5\%\ H_2}$ acid-treated Pt_3Ni/C are presented in Figs. 3 (a)–3(c), and the HR-TEM image of the acid-treated annealed$_{5\%\ H_2}$ $Pt_{2.1}Ni$/C is presented in Fig. 3(d). As shown in Figs. 3(a), 3(b) and 3(d), the morphology of the acid-treated Pt_3Ni and the acid-treated annealed$_{5\%\ H_2}$ $Pt_{2.1}Ni$ NPs are monodisperse and roughly coincide with that of the as-prepared $PtNi_{3.5}$ and the annealed$_{5\%\ H_2}$ $PtNi_{3.5}$ NPs. However, according to Fig. 3(c), with the removal of Ni element, the annealed$_{5\%\ H_2}$ acid-treated Pt_3Ni/C NPs agglomerate severely owing to an insufficient NiO protection in H_2 annealing. It is also found that the average edge length of the acid-treated Pt_3Ni NPs obviously declines to 5.88 nm after the acid treatment while there only exists a slight decrease in the average edge length (8.87 nm) of the acid-treated annealed$_{5\%\ H_2}$ $Pt_{2.1}Ni$/C. This comparison illustrates the negative effect from Ni dissolution without the protection of Pt-segregated shells as well as thermodynamically unstable heterogeneous structures, thus leading to a serious destruction in morphology.

Figures 4(a)–4(e) present the Pt 4f XPS spectra of the as-prepared $PtNi_{3.5}$, the acid-treated Pt_3Ni, annealed$_{5\%\ H_2}$ $PtNi_{3.5}$, the acid-treated annealed$_{5\%\ H_2}$ $Pt_{2.1}Ni$, and the annealed$_{5\%\ H_2}$ acid-treated Pt_3Ni. The Pt $4f_{7/2}$ and Pt $4f_{5/2}$ intense doublet were then deconvoluted to the corresponding doublets of different valence states, and the as-prepared $PtNi_{3.5}$ nanoparticles with Pt partially oxidized are initially composed of Pt^0, Pt^{2+}, and Pt^{4+}. The position and proportion of Pt^0, Pt^{2+}, and Pt^{4+} compositions obtained from corresponding fitting results have been summarized in Table S2 (in ESM). Based on the XPS results, the

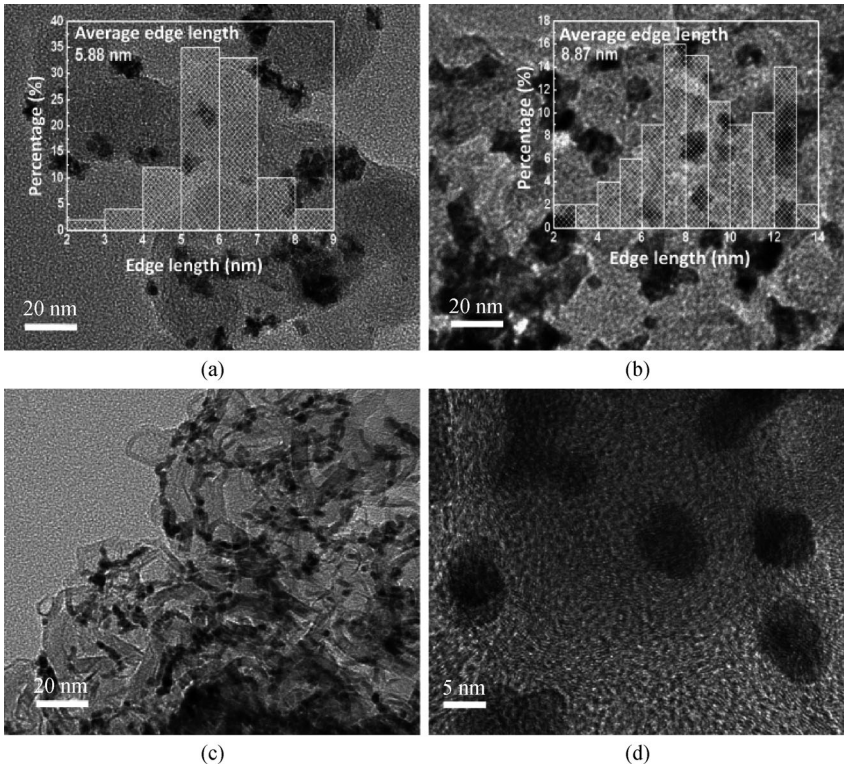

Fig. 3 Morphology analysis.

(a) TEM image of acid-treated Pt_3Ni/C; (b) acid-treated annealed$_{5\%\ H_2}$ $Pt_{2.1}Ni$/C; (c) annealed$_{5\%\ H_2}$ acid-treated Pt_3Ni/C; (d) HR-TEM image of acid-treated annealed$_{5\%\ H_2}$ $Pt_{2.1}Ni$/C.

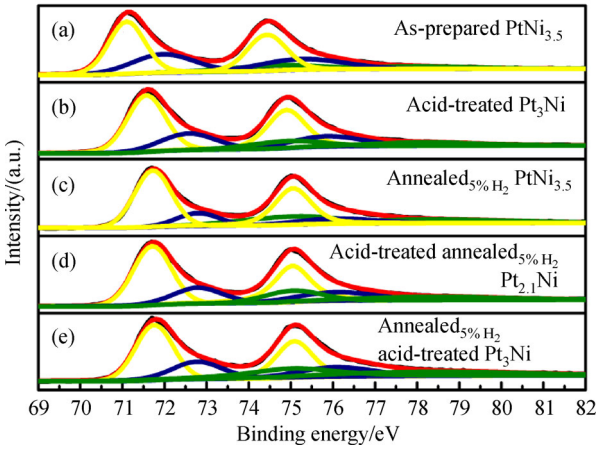

Fig. 4 Pt 4f XPS spectra (black), the doublets corresponding to Pt^0 (yellow), Pt^{2+} (blue) and Pt^{4+} (green) as well as the fitting results (red).
(a) As-prepared $PtNi_{3.5}$; (b) acid-treated Pt_3Ni; (c) annealed$_{5\%\ H_2}$ $PtNi_{3.5}$; (d) acid-treated annealed$_{5\%\ H_2}$ $Pt_{2.1}Ni$; (e) annealed$_{5\%\ H_2}$ acid-treated Pt_3Ni.

Pt^0 $4f_{7/2}$ peak of the as-prepared $PtNi_{3.5}$ NPs appears at 71.1 eV, which is similar to that of pure Pt [34] and may indicate their poor alloy degree. After being annealed, the Pt^0 $4f_{7/2}$ peak shifts positively to around 71.72 eV, demonstrating a change of outer electronic structures which decreases the d-band center of Pt atoms [35–37]. Accompanied with the downshift of d-band center, the adsorption of oxygenated intermediated products on Pt decreases, resulting in an enhanced ORR activity [38,39]. A positive shift of 0.47 eV for the acid-treated Pt_3Ni relative to the as-prepared $PtNi_{3.5}$ mainly results from the fact that after the acid treatment, erratic grains are removed and stable uniform alloys are exposed. However, the acid treatment still has limited effect on Pt outer electronic structures compared with thermal annealing.

In contrast to bare reduction of Ni^{2+}, a certain amount of highly-charged Pt element have been reduced by H_2, thus resulting in the increase in the amount of Pt^0 in $PtNi_{3.5}$ after being annealed under H_2 (Table S2, in ESM). The reason for this is that Ni has a much higher affinity for oxygen compared to Pt (NiO_x formation energy of – 2.54 eV per O versus PtO, PtO_2 formation energies of – 0.41 and – 0.63 eV per O) [40], and the reduction of PtO_x may result in both the H_2 reduction effects and the replacement of Pt in PtO_x with Ni atoms [41]. Owing to the formation of Ni-segregated outer shells and the higher oxygen affinity of Ni, the segregated Pt at inner shells mainly compose of stable Pt^0, evidenced by the same percentage of Pt^0 preserved in the acid-treated annealed$_{5\%\ H_2}$ $Pt_{2.1}Ni$ after acid pickling. Interestingly, it is found that the proportion of Pt^0 in the acid-treated Pt_3Ni/C decreases after being annealed, indicating an outward segregation of PtO_x. Combined with the Ni 2p XPS results, an outward segregation of oxides accompanied with the reduction of highly-charged Pt and Ni during H_2 anneal process is confirmed. Menning et al. [42] predicted a thermodynamically stable 3d metal-Pt-Pt surface structure in O_2, and it is speculated that this 3d metal-Pt-Pt surface structure may also be stable in the presence of O atoms in the near surface, thus forming a NiO-Pt double shells structure. It is also noted that compared with the as-prepared $PtNi_{3.5}$, the outward segregation of both NiO and PtO_x become conspicuous in the acid-treated Pt_3Ni during the H_2 thermal annealing. It is presumed in this paper that the outward segregation of oxides in the as-prepared $PtNi_{3.5}$ is driven by the decrease of oxides concentration on surface owing to the reduction by H_2. The removal of oxides on the acid-treated Pt_3Ni surface during the acid pickling results in the initial decrease of oxides concentration. Therefore, the tendency of outward segregation of oxides increases and the added oxides segregation could cover up the effect from H_2 reduction.

Figure 5 exhibits the XRD patterns measured from the as-prepared $PtNi_{3.5}$, the acid-treated Pt_3Ni, the annealed$_{5\%\ H_2}$ $PtNi_{3.5}$, the acid-treated annealed$_{5\%\ H_2}$ $Pt_{2.1}Ni$, and the annealed$_{Ar}$ $PtNi_{3.5}$ as well as standard Pt, Ni, and NiO crystals (reference: Pt PDF No. 04-0802, Ni PDF No. 04-0850 and NiO PDF No. 47-1049). There exist two separate peaks for NiO at $2\theta = 37.2°$ and 79.4° in the as-prepared $PtNi_{3.5}$. After the subsequent thermal or acid treatment, the patterns for the NiO phase disappear. The reflections of the as-prepared $PtNi_{3.5}$ are broad and asymmetric, indicating the formation of a heterogeneous structure. The removal of erratic gains and the Ni-rich phase in the as-prepared $PtNi_{3.5}$ through the acid pickling results in more symmetric reflections in the XRD pattern of the acid-treated Pt_3Ni. Considering the thermal annealing under different gaseous environments, both high alloy degree were attained, evidenced by a decrease in the full width at half maximum (FWHM) in the {111} reflections of both the annealed$_{5\%\ H_2}$ $PtNi_{3.5}$ and the annealed$_{Ar}$ $PtNi_{3.5}$ (Table 2). Compared with the annealed$_{Ar}$ $PtNi_{3.5}$, the annealed$_{5\%\ H_2}$ $PtNi_{3.5}$ attains a higher alloy degree, indicating an intense oxides and metal interdiffusion under

Table 2 XRD results of the as-prepared $PtNi_{3.5}$, the acid-treated Pt_3Ni, the annealed$_{5\%\ H_2}$ $PtNi_{3.5}$, the acid-treated annealed$_{5\%\ H_2}$ $Pt_{2.1}Ni$, and the annealed$_{Ar}$ $PtNi_{3.5}$

Sample	FWHM of {111} facets/(°)	lattice spacing of {111} facets/nm
As-prepared $PtNi_{3.5}/C$	2.063	0.216
Acid-treated Pt_3Ni/C	2.436	0.221
Annealed$_{5\%\ H_2}$ $PtNi_{3.5}/C$	1.738	0.215
Acid-treated annealed$_{5\%\ H_2}$ $Pt_{2.1}Ni/C$	1.601	0.217
Annealed$_{Ar}$ $PtNi_{3.5}/C$	1.992	0.216

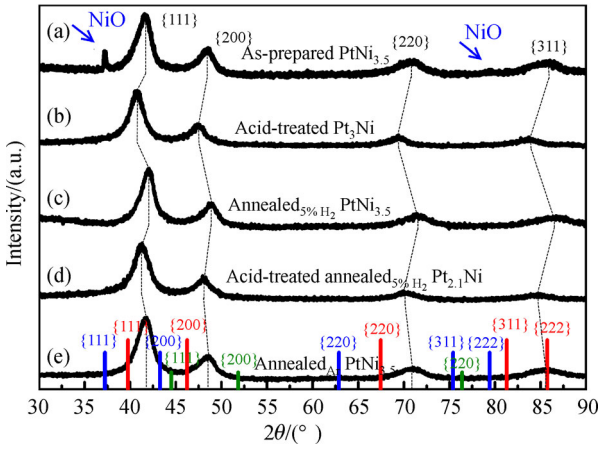

Fig. 5 XRD patterns.
(a) As-prepared $PtNi_{3.5}$; (b) acid-treated Pt_3Ni; (c) annealed$_{5\%\ H_2}$ $PtNi_{3.5}$; (d) acid-treated annealed$_{5\%\ H2}$ $Pt_{2.1}Ni$; (e) annealed$_{Ar}$ $PtNi_{3.5}$ (Blue columns correspond to NiO (PDF No. 47-1049), red columns to Pt (PDF No. 04-0802), and green columns to pure Ni (PDF No. 04-0850)).

the H_2 environment. It is noted that the formed double-shell structure causes the asymmetry of XRD peaks as measured from the annealed$_{5\%\ H_2}$ $PtNi_{3.5}$ compared with more symmetric peaks from solid solution Pt-Ni alloy by thermal annealing under pure Ar environment. Moreover, owing to the interdiffusion, homogeneous Pt-Ni alloy cores are formed for the acid-treated annealed$_{5\%\ H_2}$ $Pt_{2.1}Ni$ samples, which gives rise to the decline of crystalline interplanar space (Table 2, from 0.221 nm to 0.217 nm). The lattice contraction indicates the change in lattice strain, thus influencing the electronic structure, as convinced by XPS results.

The ORR catalytic activities of the acid-treated Pt_3Ni/C and the acid-treated annealed$_{5\%\ H_2}$ $Pt_{2.1}Ni/C$ were evaluated by CV and LSV and are recorded in Fig. 6(a). The calculated area- and mass- specific activities are displayed in Fig. 6(b). With the exposure of {111} facets in quasi-octahedrons and truncated octahedrons, enhanced ORR activities are observed for both the acid-treated Pt_3Ni/C and the acid-treated annealed$_{5\%\ H_2}$ $Pt_{2.1}Ni/C$ relative to commercial Pt/C. Both the adsorptive peak and shape of CV curves for hydrogenated species vary before and after annealing, which is related to different surface compositions or structures. The ECSA was calculated based on the adsorption of hydrogenated species (Section 2). It is concluded that the ECSA of the acid-treated Pt_3Ni/C (52.9 m^2/g_{Pt}) is larger than that of the acid-treated annealed$_{5\%\ H_2}$ $Pt_{2.1}Ni/C$ (42.6 m^2/g_{Pt}), demonstrating a loss of electrochemical active sites during the thermal annealing. However, owing to the changes in Pt electronic structure, the acid-treated annealed$_{5\%\ H_2}$ $Pt_{2.1}Ni/C$ exhibits a higher ORR activity with an area-specific activity of 2.91 mA/cm^2 and a mass-specific activity of 1.24 A/mg_{Pt} at 0.9 V versus the RHE, which are, respectively, 13.2 and 9.5 times of that for commercial Pt/C, and 4.2 and 3.4 times of that for the acid-treated Pt_3Ni/C. The acid-treated Pt_3Ni/C, the acid-treated annealed$_{5\%\ H_2}$ $Pt_{2.1}Ni/C$, and commercial Pt/C were further used as the cathodic catalyst for fuel cell performance tests. A Pt loading of 0.1 mg/cm^2 was used on both sides of the three as-fabricated MEAs. As observed in Fig. 6(d), both the acid-treated Pt_3Ni/C and the acid-treated annealed$_{5\%\ H_2}$ $Pt_{2.1}Ni/C$ possess enhanced cell performances compared with that of commercial Pt/C, especially in the high voltage region, where electrochemical polarization dominates. The current density at 0.6 V and the maximum power density when using the acid-treated annealed$_{5\%\ H_2}$ $Pt_{2.1}Ni/C$ as the cathode catalyst reach 975.8 mA/cm^2 and 679.8 mW/cm^2 under H_2/air, respectively.

The sustaining dissolution of Ni atoms from Pt-Ni alloy NPs at low PH values and high electrochemical potentials will lead to the loss of {111} facets and changes of surface composition, thus resulting in a rapid decrease in the ORR activity. The evaluation of Pt content on the surface of homogeneous Pt-Ni alloy is regarded as a prevalent method to prevent Ni erosion. The acquired images in Fig. 1(b-8) demonstrate a Pt-rich inner shell after H_2 annealing, and it is believed an enhanced durability should be observed for the acid-treated annealed$_{5\%\ H_2}$ $Pt_{2.1}Ni/C$. After the ADT, the mass-specific activities of the acid-treated annealed$_{5\%\ H_2}$ $Pt_{2.1}Ni/C$ remains 80.2%, 57.8%, 51.0%, 49.4%, and 45.4% after 3000, 5000, 12000, 20000, and 30000 cycles, demonstrating a great enhancement compared with the acid-treated Pt_3Ni/C (mass specific activity loss by 60.9% after 5000 cycles durability test). The preserved mass specific activity after the 30000 cycles of durability test for the acid-treated annealed$_{5\%\ H_2}$ $Pt_{2.1}Ni/C$ corresponds to 0.56 A/mg_{Pt} and remains 4.3 times of that for commercial Pt/C.

4 Conclusions

In conclusion, truncated octahedral $PtNi_{3.5}$ alloy nanocatalysts that consisted of homogeneous Pt-Ni alloy cores enclosed by NiO-Pt double-shells were successfully synthesized through thermally annealing defective heterogeneous $PtNi_{3.5}$ alloys under a H_2 environment. As confirmed by the TEM, HR-TEM, and HAADF-STEM results, the transformation in morphology from defective structure to energetically favorable truncated octahedrons is driven by thermodynamical effects while the redistribution of Pt and Ni driven by the gaseous effect, thus resulting in the formation of double shells. The effect of double-shell structure was further analyzed by XRD and XPS, which confirmed a Pt-rich inner shell mainly

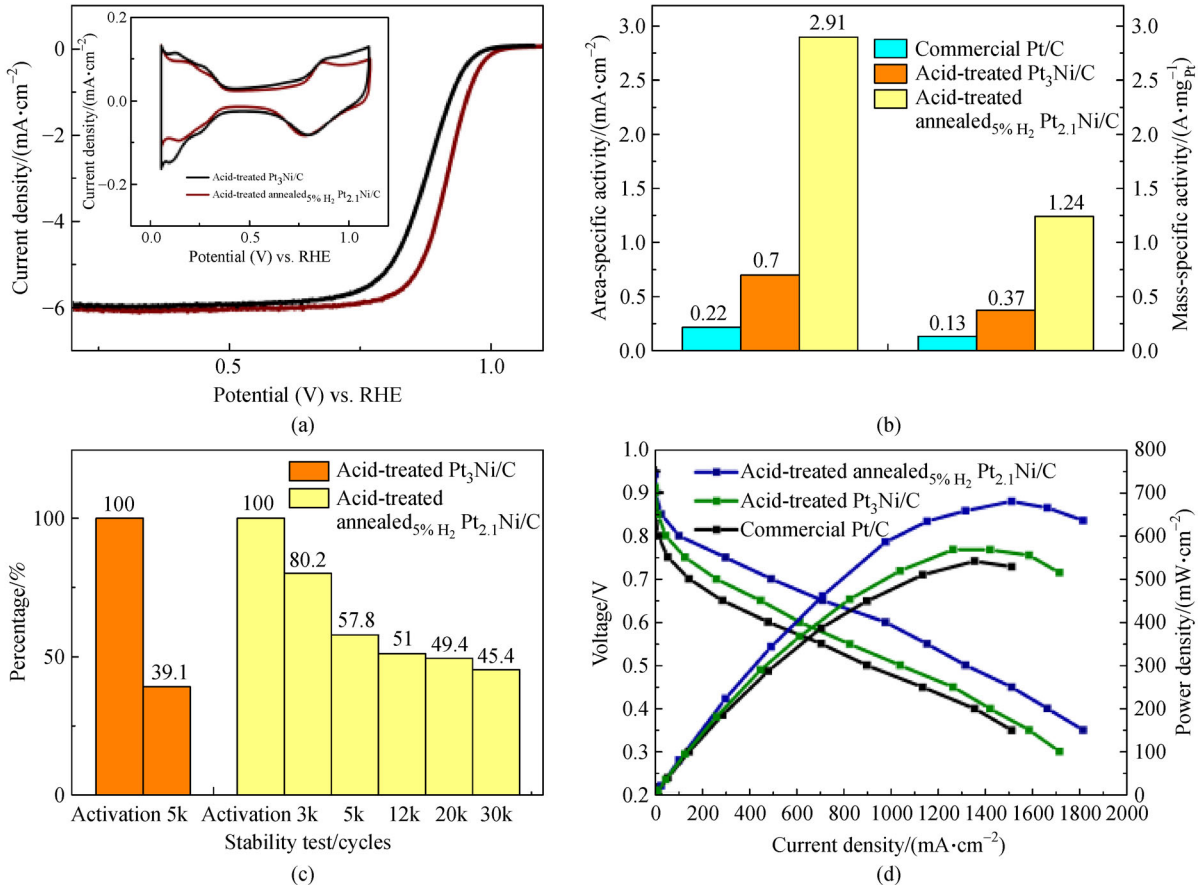

Fig. 6 Electrochemical results of acid-treated Pt_3Ni/C and acid-treated annealed$_{5\% H_2}$ $Pt_{2.1}Ni/C$.
(a) CV and LSV curves; (b) area- (left) and mass- (right) specific activity; (c) percentage of mass specific activity remained after stability test; (d) single cell tests under H_2/air.

compose of Pt^0 as well as the existence of a NiO-segregated outer shell for mitigating the agglomeration during the thermal annealing. It is also presumed that the formation of NiO-Pt double-shells was the result of the oxides surface segregation driven by oxides concentration gradient. Both the formation of Pt-segregated shells exposed by acid treatment and the high alloy degree obtained during the H_2 annealing process lead to the changes in surface composition, morphology, as well as Pt electronic structures, which strongly point toward enhancements in the ORR activity and durability. Electrochemical measurements proved that both the ORR activity and durability on dealloyed core-shell truncated octahedral $Pt_{2.1}Ni$ NPs were remarkably promoted, which reached 2.91 mA/cm^2 and 1.24 A/mg$_{Pt}$ in area- and mass-specific activity, respectively. After 30000 cycles of ADT, the mass-specific activity decreased to 0.56 A/mg$_{Pt}$. The fabricated MEA using dealloyed core-shell truncated octahedral $Pt_{2.1}Ni$ NPs as the cathodic catalyst possessed an increase of 138.4 mW/cm^2 in the maximum power density relative to that of commercial Pt/C. It is believed that the acid treatment after thermal annealing can be considered as a novel dealloying method for non-noble metal-rich Pt-based alloys, and the well-controlled synthesis of dealloyed core-shell truncated octahedral Pt-Ni alloys through thermal annealing will provide an ingenious strategy for highly active and durable Pt-based bimetallic ORR electrocatalysts.

Acknowledgements This work was financially supported by the National Key R&D Program of China (No. 2016YFB0101201) and the National Natural Science Foundation of China (Grant No. 21533005).

Electronic Supplementary Material Supplementary material is available in the online version of this article at https://doi.org/10.1007/s11708-020-0667-2 and is accessible for authorized users.

References

1. Gasteiger H A, Kocha S S, Sompalli B, Wagner F T. Activity benchmarks and requirements for Pt, Pt-alloy, and non-Pt oxygen reduction catalysts for PEMFCs. Applied Catalysis B: Environmental, 2005, 56(1–2): 9–35
2. Papageorgopoulos D. Fuel cells R&D overview. 2018–06–13,

available at the website of hydrogen.energy.gov
3. Shao M, Chang Q, Dodelet J P, Chenitz R. Recent advances in electrocatalysts for oxygen reduction reaction. Chemical Reviews, 2016, 116(6): 3594–3657
4. Wang Y J, Zhao N, Fang B, Li H, Bi X T, Wang H. Carbon-supported Pt-based alloy electrocatalysts for the oxygen reduction reaction in polymer electrolyte membrane fuel cells: particle size, shape, and composition manipulation and their impact to activity. Chemical Reviews, 2015, 115(9): 3433–3467
5. Chaudhari N K, Joo J, Kim B, Ruqia B, Choi S I, Lee K. Recent advances in electrocatalysts toward the oxygen reduction reaction: the case of PtNi octahedra. Nanoscale, 2018, 10(43): 20073–20088
6. Arán-Ais R M, Dionigi F, Merzdorf T, Gocyla M, Heggen M, Dunin-Borkowski R E, Gliech M, Solla-Gullón J, Herrero E, Feliu J M, Strasser P. Elemental anisotropic growth and atomic-scale structure of shape-controlled octahedral Pt-Ni-Co alloy nanocatalysts. Nano Letters, 2015, 15(11): 7473–7480
7. Salgado J R C, Antolini E, Gonzalez E R. Structure and activity of carbon-supported Pt-Co electrocatalysts for oxygen reduction. Journal of Physical Chemistry B, 2004, 108(46): 17767–17774
8. Stamenkovic V, Mun B S, Mayrhofer K J J, Ross P N, Markovic N M, Rossmeisl J, Greeley J, Nørskov J K. Changing the activity of electrocatalysts for oxygen reduction by tuning the surface electronic structure. Angewandte Chemie International Edition, 2006, 45(18): 2897–2901
9. Zhang J, Fang J. A general strategy for preparation of Pt 3d-transition metal (Co, Fe, Ni) nanocubes. Journal of the American Chemical Society, 2009, 131(51): 18543–18547
10. Zhu Z, Zhai Y, Dong S. Facial synthesis of PtM (M = Fe, Co, Cu, Ni) bimetallic alloy nanosponges and their enhanced catalysis for oxygen reduction reaction. ACS Applied Materials & Interfaces, 2014, 6(19): 16721–16726
11. Choi S I, Xie S, Shao M, Odell J H, Lu N, Peng H C, Protsailo L, Guerrero S, Park J, Xia X, Wang J, Kim M J, Xia Y. Synthesis and characterization of 9 nm Pt-Ni octahedra with a record high activity of 3.3 A/mg_{Pt} for the oxygen reduction reaction. Nano Letters, 2013, 13(7): 3420–3425
12. Chou S W, Lai Y R, Yang Y Y, Tang C Y, Hayashi M, Chen H C, Chen H L, Chou P T. Uniform size and composition tuning of PtNi octahedra for systematic studies of oxygen reduction reactions. Journal of Catalysis, 2014, 309: 343–350
13. Cui C, Gan L, Li H H, Yu S H, Heggen M, Strasser P. Octahedral PtNi nanoparticle catalysts: exceptional oxygen reduction activity by tuning the alloy particle surface composition. Nano Letters, 2012, 12(11): 5885–5889
14. Gan L, Heggen M, Rudi S, Strasser P. Core-shell compositional fine structures of dealloyed Pt_xNi_{1-x} nanoparticles and their impact on oxygen reduction catalysis. Nano Letters, 2012, 12(10): 5423–5430
15. Park J, Liu J, Peng H, Figueroa-Cosme L, Miao S, Choi S I, Bao S, Yang X, Xia Y. Coating Pt-Ni octahedra with ultrathin Pt shells to enhance the durability without compromising the activity toward oxygen reduction. ChemSusChem, 2016, 9(16): 2209–2215
16. Wu J, Yang H. Synthesis and electrocatalytic oxygen reduction properties of truncated octahedral Pt_3Ni nanoparticles. Nano Research, 2011, 4(1): 72–82
17. Wu J, Zhang J, Peng Z, Yang S, Wagner F T, Yang H. Truncated octahedral Pt_3Ni oxygen reduction reaction electrocatalysts. Journal of the American Chemical Society, 2010, 132(14): 4984–4985
18. Zhang C, Hwang S Y, Trout A, Peng Z. Solid-state chemistry-enabled scalable production of octahedral Pt-Ni alloy electrocatalyst for oxygen reduction reaction. Journal of the American Chemical Society, 2014, 136(22): 7805–7808
19. Zhang J, Yang H, Fang J, Zou S. Synthesis and oxygen reduction activity of shape-controlled Pt_3Ni nanopolyhedra. Nano Letters, 2010, 10(2): 638–644
20. Wu J, Qi L, You H, Gross A, Li J, Yang H. Icosahedral platinum alloy nanocrystals with enhanced electrocatalytic activities. Journal of the American Chemical Society, 2012, 134(29): 11880–11883
21. Beermann V, Gocyla M, Kühl S, Padgett E, Schmies H, Goerlin M, Erini N, Shviro M, Heggen M, Dunin-Borkowski R E, Muller D A, Strasser P. Tuning the electrocatalytic oxygen reduction reaction activity and stability of shape-controlled Pt-Ni nanoparticles by thermal annealing-elucidating the surface atomic structural and compositional changes. Journal of the American Chemical Society, 2017, 139(46): 16536–16547
22. Chen C, Kang Y, Huo Z, Zhu Z, Huang W, Xin H L, Snyder J D, Li D, Herron J A, Mavrikakis M, Chi M, More K L, Li Y, Markovic N M, Somorjai G A, Yang P, Stamenkovic V R. Highly crystalline multimetallic nanoframes with three-dimensional electrocatalytic surfaces. Science, 2014, 343(6177): 1339–1343
23. Wang D, Xin H L, Hovden R, Wang H, Yu Y, Muller D A, DiSalvo F J, Abruña H D. Structurally ordered intermetallic platinum-cobalt core-shell nanoparticles with enhanced activity and stability as oxygen reduction electrocatalysts. Nature Materials, 2013, 12(1): 81–87
24. Gocyla M, Kuehl S, Shviro M, Heyen H, Selve S, Dunin-Borkowski R E, Heggen M, Strasser P. Shape stability of octahedral PtNi nanocatalysts for electrochemical oxygen reduction reaction studied by *in situ* transmission electron microscopy. ACS Nano, 2018, 12 (6): 5306–5311
25. Gan L, Heggen M, Cui C, Strasser P. Thermal facet healing of concave octahedral Pt-Ni nanoparticles imaged *in situ* at the atomic scale: implications for the rational synthesis of durable high-performance ORR electrocatalysts. ACS Catalysis, 2016, 6(2): 692–695
26. Wang G, Van Hove M A, Ross P N, Baskes M I. Monte Carlo simulations of segregation in Pt-Ni catalyst nanoparticles. Journal of Chemical Physics, 2005, 122(2): 024706
27. Calle-Vallejo F, Pohl M D, Reinisch D, Loffreda D, Sautet P, Bandarenka A S. Why conclusions from platinum model surfaces do not necessarily lead to enhanced nanoparticle catalysts for the oxygen reduction reaction. Chemical Science (Cambridge), 2017, 8 (3): 2283–2289
28. Patrick B, Ham H C, Shao-Horn Y, Allard L F, Hwang G S, Ferreira P J. Atomic structure and composition of "Pt_3Co" nanocatalysts in fuel cells: an aberration-corrected STEM HAADF study. Chemistry of Materials, 2013, 25(4): 530–535
29. Martinez U, Komini Babu S, Holby E F, Zelenay P. Durability challenges and perspective in the development of PGM-free electrocatalysts for the oxygen reduction reaction. Current Opinion in Electrochemistry, 2018, 9: 224–232
30. Hartl K, Nesselberger M, Mayrhofer K J J, Kunz S, Schweinberger

F F, Kwon G H, Hanzlik M, Heiz U, Arenz M. Electrochemically induced nanocluster migration. Electrochimica Acta, 2010, 56(2): 810–816

31. Liu C, Wu X, Klemmer T, Shukla N, Weller D, Roy A G, Tanase M, Laughlin D. Reduction of sintering during annealing of FePt nanoparticles coated with iron oxide. Chemistry of Materials, 2005, 17(3): 620–625
32. Gao M Y, Li A D, Zhang J L, Kong J Z, Liu X J, Li X F, Wu D. Fabrication and magnetic properties of FePt nanoparticle assemblies embedded in MgO-matrix systems. Journal of Sol-Gel Science and Technology, 2014, 71(2): 283–290
33. Zeynali H, Sebt S A, Arabi H, Akbari H, Hosseinpour-Mashkani S M, Rao K V. Synthesis and characterization of FePt/NiO core-shell nanoparticles. Journal of Inorganic and Organometallic Polymers and Materials, 2012, 22(6): 1314–1319
34. Beard B C, Ross P N. Platinum-titanium alloy formation from high-temperature reduction of a titania-impregnated platinum catalyst: implications for strong metal-support interaction. Journal of Physical Chemistry, 1986, 90(26): 6811–6817
35. Choi S I, Lee S U, Kim W Y, Choi R, Hong K, Nam K M, Han S W, Park J T. Composition-controlled PtCo alloy nanocubes with tuned electrocatalytic activity for oxygen reduction. ACS Applied Materials & Interfaces, 2012, 4(11): 6228–6234
36. Tan X, Prabhudev S, Kohandehghan A, Karpuzov D, Botton G A, Mitlin D. Pt-Au-Co alloy electrocatalysts demonstrating enhanced activity and durability toward the oxygen reduction reaction. ACS Catalysis, 2015, 5(3): 1513–1524
37. Wakisaka M, Mitsui S, Hirose Y, Kawashima K, Uchida H, Watanabe M. Electronic structures of Pt-Co and Pt-Ru alloys for CO-tolerant anode catalysts in polymer electrolyte fuel cells studied by EC-XPS. Journal of Physical Chemistry B, 2006, 110(46): 23489–23496
38. Kitchin J R, Nørskov J K, Barteau M A, Chen J G. Modification of the surface electronic and chemical properties of Pt(111) by subsurface 3d transition metals. Journal of Chemical Physics, 2004, 120(21): 10240–10246
39. Zhang J, Vukmirovic M B, Xu Y, Mavrikakis M, Adzic R R. Controlling the catalytic activity of platinum-monolayer electrocatalysts for oxygen reduction with different substrates. Angewandte Chemie International Edition, 2005, 44(14): 2132–2135
40. Li W X, Österlund L, Vestergaard E K, Vang R T, Matthiesen J, Pedersen T M, Lægsgaard E, Hammer B, Besenbacher F. Oxidation of Pt(110). Physical Review Letters, 2004, 93(14): 146104
41. Ahmadi M, Behafarid F, Cui C, Strasser P, Cuenya B R. Long-range segregation phenomena in shape-selected bimetallic nanoparticles: chemical state effects. ACS Nano, 2013, 7(10): 9195–9204
42. Menning C A, Chen J G. Regenerating Pt-3d-Pt model electrocatalysts through oxidation-reduction cycles monitored at atmospheric pressure. Journal of Power Sources, 2010, 195(10): 3140–3144